Mineralogical Magazine (2025), 1–11
doi:10.1180/mgm.2025.10114

CAMBRIDGE UNIVERSITY PRESS

Article

Ferro-bosiite, $NaFe^{3+}_3(Al_4Fe^{2+}_2)(Si_6O_{18})(BO_3)_3(OH)_3O$, a new mineral species of the tourmaline supergroup

Ferdinando Bosi[1], Alessandra Altieri[1], Henrik Skogby[2], Federico Pezzotta[3], Ulf Hålenius[2], Gioacchino Tempesta[4], Paolo Ballirano[1], Tomáš Flégr[5] and Jan Cempírek[5]

[1]Department of Earth Sciences, Sapienza University of Rome, Rome, Italy; [2]Department of Geosciences, Swedish Museum of Natural History, Stockholm, Sweden; [3]MUM – Mineralogical Museum "Luigi Celleri", San Piero in Campo, Campo nell'Elba, Livorno, Italy; [4]Dipartimento di Scienze della Terra e Geoambientali, Università degli Studi di Bari Aldo Moro, Bari, Italy; and [5]Department of Geological Sciences, Faculty of Science, Masaryk University, Brno, Czech Republic

Abstract

Ferro-bosiite, $NaFe^{3+}_3(Al_4Fe^{2+}_2)(Si_6O_{18})(BO_3)_3(OH)_3O$, is a new mineral of the tourmaline supergroup. It was found in a giant collapsed cavity discovered in the Marina granitic pegmatite, at the Mavuco locality, Alto Ligonha, Mozambique. Ferro-bosiite occurs as a black acicular late-stage overgrowth at the analogous pole of a multicoloured fluor-elbaite crystal. The black crystals, with a vitreous lustre, have a brown streak, conchoidal fracture and a Mohs hardness of ~7. Ferro-bosiite is uniaxial (–), with refractive indices $\omega = 1.675(5)$ and $\varepsilon = 1.645(5)$. It has trigonal symmetry, space group $R3m$, $a = 16.0499(5)$ Å, $c = 7.2977(2)$ Å, $V = 1628.03(11)$ Å^3, $Z = 3$ and calculated density = 3.216 g/cm^3. The crystal structure was refined to $R_1 = 2.55\%$ using 1547 unique reflections collected with Mo$K\alpha$ X-ray intensity data. Crystal-chemical analysis resulted in the empirical crystal-chemical formula: $^{X}(Na_{0.99}K_{0.02})_{\Sigma1.01}{}^{Y}(Fe^{3+}_{1.56}V^{3+}_{0.02}Mg_{1.01}Fe^{2+}_{0.20}Mn^{2+}_{0.03}Ti_{0.16}Li_{0.02})_{\Sigma3.00}{}^{Z}(Al_{4.32}Fe^{3+}_{0.41}Fe^{2+}_{1.22}Mg_{0.05})_{\Sigma6.00}{}^{T}[(Si_{5.99}Al_{0.01})_{\Sigma6.00}O_{18}](BO_3)_3{}^{O(3)}(OH)_3{}^{O(1)}[O_{0.62}(OH)_{0.34}F_{0.04}]_{\Sigma1.00}$.
Ferro-bosiite is an oxy-species belonging to alkali group 3 of the tourmaline supergroup. It is related to bosiite by the substitution $^{Z}Fe^{2+} \leftrightarrow {}^{Z}Mg$. The new mineral has been approved by the International Mineralogical Association's Commission on New Minerals, Nomenclature and Classification (IMA 2020-069). Ferro-bosiite forms part of a continuous solid-solution trend from Fe^{3+}-rich oxy-dravite to dutrowite, driven by increasing Fe^{3+} and Ti, and *X*-site vacancies. At its type locality, ferro-bosiite formed during late-stage interaction with B-rich hydrothermal fluids that became enriched in Fe and Mg, probably due to a distinct fluid phase active after the collapse of a giant cavity.

Keywords: ferro-bosiite; new mineral species; crystal-structure refinement; electron microprobe; Mössbauer spectroscopy; infrared spectroscopy; optical absorption spectroscopy; micro-Laser Induced Breakdown Spectroscopy; pegmatite pocket collapse; late-stage fluids; Marina pegmatite; Mozambique

(Received 21 April 2025; accepted 24 June 2025; Accepted Manuscript published online: 4 August 2025)

Introduction

Tourmalines are complex borosilicates with general chemical formula $XY_3Z_6T_6O_{18}(BO_3)_3V_3W$, where X = Na^+, K^+, Ca^{2+} and □ (= vacancy); Y = Al^{3+}, Fe^{3+}, Cr^{3+}, V^{3+}, Mg^{2+}, Fe^{2+}, Mn^{2+} and Li^+; Z = Al^{3+}, Fe^{3+}, Cr^{3+}, V^{3+}, Mg^{2+} and Fe^{2+}; T = Si^{4+}, Al^{3+} and B^{3+}; B = B^{3+}; V = $(OH)^-$ and O^{2-}; W = $(OH)^-$, F^- and O^{2-} (Hawthorne and Henry, 1999; Henry *et al.*, 2011; Bačík and Fridrichová, 2021). Note that unitalicised letters X, Y, Z and B represent groups of cations hosted at the $^{[9]}X$, $^{[6]}Y$, $^{[6]}Z$, $^{[4]}T$ and $^{[3]}B$ crystallographic sites (letters italicised), whereas the letters V and W represent groups of anions accommodated at the [3]-coordinated O(3) and O(1) crystallographic sites, respectively. The dominance of specific ions at one or more sites of the structure gives rise to a range of distinct mineral species including ferro-bosiite. As of October 2025, the tourmaline supergroup contains 42 approved mineral species.

A formal description of the new tourmaline species ferro-bosiite is presented here. The new species and the new name have been approved by the International Mineralogical Association's Commission on New Minerals, Nomenclature and Classification (IMA 2022-069, Bosi *et al.*, 2023). Holotype material is deposited in the collections of the "Museo Universitario di Scienze della Terra" (MUST), Dipartimento di Scienze della Terra, Sapienza Università di Roma, Italy, catalogue number 33308/405.

Corresponding author: Ferdinando Bosi; Email: ferdinando.bosi@uniroma1.it
Guest Editor: Robert F. Martin

This paper is part of a collection in tribute to the work of Edward Grew at 80

Cite this article: Bosi F., Altieri A., Skogby H., Pezzotta F., Hålenius U., Tempesta G., Ballirano P., Flégr T. and Cempírek J. (2025) Ferro-bosiite, $NaFe^{3+}_3(Al_4Fe^{2+}_2)(Si_6O_{18})(BO_3)_3(OH)_3O$, a new mineral species of the tourmaline supergroup. *Mineralogical Magazine*, 1–11. https://doi.org/10.1180/mgm.2025.10114

© The Author(s), 2025. Published by Cambridge University Press on behalf of The Mineralogical Society of the United Kingdom and Ireland. This is an Open Access article, distributed under the terms of the Creative Commons Attribution licence (http://creativecommons.org/licenses/by/4.0), which permits unrestricted re-use, distribution and reproduction, provided the original article is properly cited.

Occurrence

The holotype specimen was selected from a relatively large number of tourmaline crystals found in a giant collapsed cavity (~12 m in size) discovered in the Marina granitic pegmatite, at the Mavuco locality (Alto Ligonha, Mozambique; geographic coordinates: 15°55'09.61"S, 39°00'47.05"E, ~170 m above the sea level). The Marina pegmatite is a relatively large body (at the surface it is more than 140 m long and 15 m thick) hosted in amphibolite. The pegmatite got its name for surface occurrences of gem crystals of the beryl variety *aquamarine*. A few years ago, the owner of the mining license, the Mozambique-Gems Company, started downdip exploration of the pegmatite which resulted in excavation of a large open-pit that continued into some tunnels. At depth, the pegmatite rapidly changed textures and mineralogy; indeed, the core zone which at the surface was characterised by large masses of white to pale rose quartz associated with schorl and blue beryl (*aquamarine*), changed at depth. It became a coarse-grained rock composed of albite (variety *cleavelandite*; see Martin, 2024) with minor quartz and local amazonitic microcline, with abundant accessory black and multicoloured tourmaline prisms (from a few cm up to over 30 cm), rare large tabular crystals of pale pink beryl with a pale green core, and granular masses of silvery to purplish Li-rich mica. At a depth of ~25 m, a giant collapsed cavity was encountered. This cavity was mostly filled with collapsed crystals and rocks partially cemented by a thick crust of whitish late-stage chalcedony. The collapsed material is mostly composed of *cleavelandite* (in large 'pillows') and large milky quartz crystals (in aggregates up to over a ton in weight). In the collapsed material, several hundreds of kilos of yellow to pink tourmaline crystals (from a few cm up to ~20 cm) covered by a thick black tourmaline overgrowth, were discovered. Among the other minerals found in the collapsed materials, it is noteworthy that there were several tens of kilograms of native bismuth and purple fluorite in octahedral crystals up to 20 cm across. After the partial removal of the collapsed materials, a cavity over 12 m long and up to 5–6 m wide was revealed. The vertical extent of the original cavity is uncertain as the collapse affected the roof of the pocket, the intermediate and the border zones of the pegmatite and even the amphibolitic host rock. The collapse structure extends for at least 10–12 m.

The multicolour tourmaline crystals formed together with the *cleavelandite* in the cavity before the collapse and grew as prisms in the direction of the antilogous pole, with a steep pyramidal termination. These crystals were damaged and broke off from the matrix during the pocket rupture; they were later overgrown by a thick (up to 3–4 mm) black tourmaline. The late-stage overgrowth covered all of the tourmaline surfaces, including the prism faces, the steep pyramidal faces at the antilogous pole and the broken surfaces. Our investigation showed that the ferro-bosiite composition is strictly confined to the overgrowths on analogous pole surfaces, such as the bottom of the crystals broken off from the matrix; the remaining tourmaline surfaces are covered by black overgrowth of dravitic composition along with bosiite.

Appearance, physical and optical properties

Ferro-bosiite occurs as a black acicular late-stage overgrowth (up to 4 mm thick and chemically heterogeneous) at the analogous pole of a multicoloured fluor-elbaite crystal of several centimetres in length (Fig. 1). The black crystals, with a vitreous lustre, have a brown streak and show no fluorescence. Ferro-bosiite has a Mohs hardness of ~7, by analogy with bosiite (Ertl *et al.*, 2016) and is brittle with a conchoidal fracture. The calculated density, based on the empirical formula and unit-cell volume refined from single-crystal X-ray diffraction data, is 3.261 g/cm^3. In plane-polarised light, it is pleochroic, O = dark grey and E = pale yellow; O > E. Ferro-bosiite is uniaxial (–) with refractive indices $\omega = 1.675(5)$ and $\varepsilon = 1.645(5)$ measured by the immersion method using white light from a tungsten source. The mean index of refraction, density, and chemical composition led to a fair compatibility index (1 – $Kp/Kc = 0.069$) (Mandarino, 1981), most likely due to the strong chemical inhomogeneity occurring on a small scale.

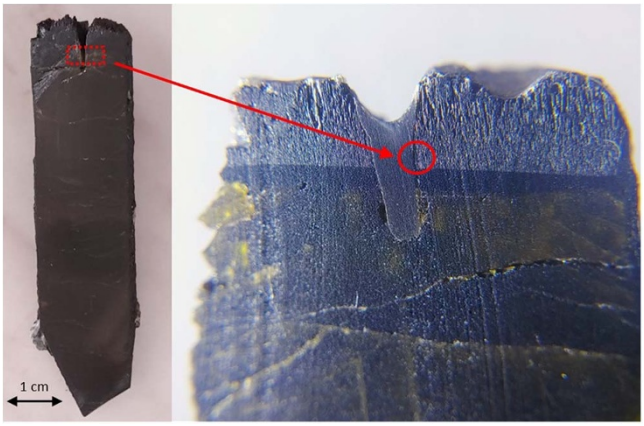

Figure 1. Photos of tourmaline from the 'Marina' pegmatite, Mavuco, Mozambique, with an overgrowth of acicular black tourmaline (red dotted rectangle) containing the holotype fragment of ferro-bosiite (red circle).

Analytical methods and results

Single-crystal X-ray diffraction (SCXRD) and structure refinement (SREF)

A representative crystal of ferro-bosiite was selected for X-ray diffraction measurements on a Bruker KAPPA APEX-II single-crystal diffractometer (Sapienza University of Rome, Earth Sciences Department), equipped with a CCD area detector (6.2 × 6.2 cm active detection area, 512 × 512 pixels) and a graphite-crystal monochromator, using Mo$K\alpha$ radiation from a fine-focus sealed X-ray tube. The sample-to-detector distance was 4 cm. A total of 1619 exposures (step = 0.4°, time/step = 20 s), covering a full reciprocal sphere, was collected using ω and φ scan modes. Final unit-cell parameters were refined using the Bruker AXS *SAINT* program on reflections with $I > 10\sigma_I$ in the range $5° < 2\theta < 73°$. The intensity data were processed and corrected for Lorentz, polarisation and background effects using the *APEX2* software program of Bruker AXS. The data were corrected for absorption using a multi-scan method (*SADABS*). The absorption correction led to a significant improvement in R_{int}. No violation of *R*3*m* symmetry was detected.

Structure refinement was done using the *SHELXL-2013* program (Sheldrick, 2015). Starting coordinates were taken from Bosi and Skogby (2013). Variable parameters included scale factor, extinction coefficient, atom coordinates, site-scattering values (for *X*, *Y* and *Z* sites) and atomic displacement factors. The crystal structure was refined as a two-component inversion twin. Attempts to refine the extinction coefficient yielded values within its standard uncertainty; thus it was not refined. A fully ionised-oxygen scattering factor and neutral cation scattering factors were used.

Table 1. Single-crystal X-ray diffraction data details for ferro-bosiite

Formula derived from SREF	$Na_{1.005}(Fe_{0.635}Mg_{0.365})_3(Al_{0.725}Fe_{0.275})_6(Si_6O_{18})(BO_3)_3(OH)_3O$
Crystal size (mm)	0.22 × 0.26 × 0.36
Space-group type	*R*3*m* (# 160)
a (Å)	16.0499(5)
c	7.2977(2)
V (Å^3)	1628.03(11)
Z	3
Axis, frame width (°), time per frame (s)	Phi-omega, 0.4, 20
Data collection temperature (K)	293(2)
Radiation, Mo*K*α (Å)	0.71073
Range for data collection, 2θ (°)	5–74
Reciprocal space range *hkl*	$-20 \le h \le 26$; $-24 \le k \le 16$; $-12 \le l \le 12$
Set of read reflections	3292
Unique reflections (all and $I > 2\sigma_I$), R_{int} (%)	1729 and 1547, 1.87
F(000)	1755
Number of refined parameters	93
Redundancy	3.25
Absorption correction method	Multiscan (*SADABS*)
Refinement method	Full-matrix last-squares on F^2
Structural refinement program	*SHELXL–2013*
Flack parameter	0.08(3)
wR_2 (%)	5.00
R_1 (%) all data	3.35
R_1 (%) for $I > 2\sigma_I$	2.55
GooF	0.989
Largest diff. peak and hole (e^-/Å^3)	−0.49 and 0.63

Notes: R_{int} = merging residual value; R_1 = discrepancy index, calculated from *F*-data; wR_2 = weighted discrepancy index, calculated from F^2-data; GooF = goodness of fit; Diff. Peaks = maximum and minimum residual electron density.

In detail, the *X* site was modelled using the Na scattering factor. The mean electron number of the *Y* site was obtained by refining occupancy of Fe *versus* Mg, and the *Z* site with Al *versus* Fe. The *T, B* and anion sites were modelled, respectively, with Si, B and O^{2-} scattering factors and with a fixed occupancy of 1, as refinement with unconstrained occupancies showed no significant deviations from this value. The position of the H atom bonded to the oxygen at the O(3) site in the structure was found in the difference-Fourier map and incorporated into the refinement model; the O(3)–H(3) bond length was restrained (by DFIX command) to be 0.97 Å with an isotropic displacement parameter constrained to be equal to 1.2 times that obtained for the O(3) site. Table 1 lists crystal data, data-collection information, and refinement details, whereas Table 2 gives the fractional atom coordinates and equivalent isotropic displacement parameters; Table 3 shows selected bond lengths. Complete structural data are provided in the deposited crystallographic information file (CIF).

Powder X-ray diffraction (PXRD)

Powder X-ray diffraction data were collected using a Bruker AXS D8 Advance diffractometer equipped with incident-beam focusing Göbel mirrors and a position-sensitive detector VÅntec-1 set to an opening angle of 6°2θ. The instrument operates in vertical θ/θ geometry in transmission mode. A small sphere (ca. 0.3 mg) of pulverised ferro-bosiite embedded in thermoplastic resin (the same sample as used for collecting a Mössbauer spectrum; see below) was mounted on the tip of a 0.3 mm diameter borosilicate glass capillary by gently heating the tip. The capillary was then fixed and aligned on a standard goniometer head (Supplementary Fig. S1). Data were collected over the 2θ range of 6–145° with a step size of 0.021798° and a counting time of 10 s per step. The Rietveld plots, resulting from the refinement of unit-cell parameters and peak shape with fixed structural data from single-crystal refinement, are provided in Supplementary Fig. S2. The refinement was performed using *Topas V6* (Bruker AXS, 2016), which implements the Fundamental Parameters Approach (FPA; Cheary and Coelho, 1992) to model peak shapes. Absorption effects were corrected using the equation of Sabine *et al.* (1998) for cylindrical samples. The refinement yielded an excellent fit, with convergence achieved at the following statistical indicators: Rwp = 0.97%, Rp = 0.75%, R_B = 0.20% and χ^2 = 1.14 (as defined by Young, 1993).

The refined unit-cell parameters, a = 16.0454(3) Å, c = 7.2939(3) Å and V = 1626.27(9) Å^3, are in very good agreement with those obtained from SCXRD (Table 1). Owing to the significant amorphous contribution from both the thermoplastic resin and the glass capillary, as well as the relatively low signal/noise ratio caused by the very small amount of sample, a full Rietveld refinement could not be performed. Nonetheless, the excellent agreement between experimental and calculated data from the single-crystal structure model (CIF of the SREF) confirms that the chemical differences between the powdered ferro-bosiite material and the crystal used for SCXRD, electron microprobe analysis and laser induced breakdown spectroscopy are minimal. Experimental and calculated *d*-spacings of the relevant reflections of ferro-bosiite are listed in Table 4.

Electron microprobe analysis (EMPA)

The crystal used for X-ray diffraction refinement was analysed by wavelength dispersive spectrometer (WDS mode) using a Cameca SX50 instrument (CNR-Istituto di Geologia Ambientale e Geoingegneria, Rome, Italy) operating at an accelerating potential of 15 kV and a sample current of 15 nA, with a 10 µm beam diameter. The following standards, X-ray *K*α lines and analyser crystals were used: jadeite (Na; TAP), periclase (Mg; TAP), orthoclase (K; PET), rutile (Ti; PET), wollastonite (Si, Ca; PET), metallic Zn and Mn (Zn, Mn; LIF), vanadinite (V; PET), fluorophlogopite (F; TAP), metallic Cr (Cr; PET), corundum (Al; TAP), and magnetite (Fe; LIF). The "PAP" routine was applied (Pouchou and Pichoir, 1991). The results (Table 5) represent mean values of six spot analyses. Calcium, Cr, Cu and Zn are below detection limits (< 0.03 wt.%).

Micro-laser induced breakdown spectroscopy (µ-LIBS)

The crystal used for X-ray diffraction refinement was analysed for Li. The latter analysis was performed using 110 mJ of energy per pulse by double pulse Q-Switched (Nd-YAG, λ = 1064 nm) laser with a 1 µs delay between the two pulses. The small spot size (7–10 µm) was obtained using a petrographic optical microscope (objective lens 10× NA 0.25 WD 14.75 mm). The LIBS spectra were acquired by an AvaSpec Fiber Optic Spectrometer (390–900 nm with 0.3 nm resolution) with a delay of 2 µs after the second pulse and were integrated for 1 ms. Quantitative data were obtained by generating a linear regression using the main Li emission line intensity (670.706 nm corresponding to resonance transition $1s^2\ 2s > 1s^2\ 2p$) particularly sensitive to Li amounts. The linear fit was made according to Bosi *et al.* (2021) and revealed Li_2O 0.03 wt.% (Table 5).

Table 2. Sites, Wyckoff positions, site occupancies, fractional atom coordinates and isotropic or equivalent-isotropic displacement parameters (in Å^2) for ferro-bosiite

Site	Wyckoff position	Site occupancy	*x*	*y*	*z*	$U_{eq/iso}$
X	3*a*	$Na_{1.005(13)}$	0	0	0.2376(5)	0.0292(11)
Y	9*b*	$Fe_{0.635(6)}Mg_{0.365(6)}$	0.12371(5)	0.06185(3)	0.63625(12)	0.01202(19)
Z	18*c*	$Al_{0.725(5)}Fe_{0.275(5)}$	0.29855(5)	0.26159(5)	0.61177(12)	0.01018(15)
B	9*b*	$B_{1.00}$	0.10981(17)	0.2196(3)	0.4564(5)	0.0113(7)
T	18c	$Si_{1.00}$	0.19098(5)	0.18927(5)	0	0.00945(15)
O(1) ≡ W	3*a*	$O_{1.00}$	0	0	0.7753(7)	0.0230(11)
O(2)	9*b*	$O_{1.00}$	0.06124(10)	0.1225(2)	0.4868(4)	0.0148(6)
O(3) ≡ V	9*b*	$O_{1.00}$	0.2636(2)	0.13182(12)	0.5125(4)	0.0179(6)
H(3)	9*b*	$H_{1.00}$	0.260(4)	0.1299(18)	0.381(3)	0.021*
O(4)	9*b*	$O_{1.00}$	0.09267(11)	0.1853(2)	0.0690(4)	0.0145(5)
O(5)	9*b*	$O_{1.00}$	0.1840(2)	0.09198(11)	0.0883(3)	0.0137(5)
O(6)	18*c*	$O_{1.00}$	0.19558(14)	0.18590(14)	0.7803(3)	0.0124(4)
O(7)	18*c*	$O_{1.00}$	0.28344(13)	0.28350(13)	0.0781(3)	0.0131(4)
O(8)	18*c*	$O_{1.00}$	0.20815(15)	0.26892(15)	0.4415(3)	0.0161(4)

*Isotropic displacement parameters (U_{iso}) for H(3) constrained to have a U_{iso} 1.2 times the U_{eq} value of the O(3) oxygen atom.

Table 3. Selected bond lengths (in Å) for ferro-bosiite

X–O(2)	2.491(4)	× 3	*Y*–O(1)	1.997(3)	
X–O(5)	2.780(3)	× 3	*Y*–O(6)	2.026(2)	× 2
X–O(4)	2.855(3)	× 3	*Y*–O(2)	2.0291(18)	× 2
<*X*–O>	2.709		*Y*–O(3)	2.144(3)	
			<*Y*–O>	2.042	
T–O(7)	1.6032(18)				
T–O(6)	1.6070(19)		*Z*–O(8)	1.924(2)	
T–O(4)	1.6271(11)		*Z*–O(6)	1.927(2)	
T–O(5)	1.6402(12)		*Z*–O(7)	1.9344(19)	
<*T*–O>	1.619		*Z*–O(8)	1.958(2)	
			Z–O(7)	1.9936(19)	
B–O(2)	1.368(5)		*Z*–O(3)	2.0025(14)	
B–O(8)	1.371(3)	× 2	<*Z*–O>	1.957	
<*B*–O>	1.370				

Mössbauer spectroscopy

A Mössbauer spectrum was collected at room temperature using a conventional spectrometer system operating in constant acceleration mode with a ^{57}Co point-source of 10 mCi in a rhodium matrix. The absorber consisted of ca 0.3 mg powdered ferro-bosiite embedded in thermoplastic resin.

Data were collected over 1024 channels and were folded and calibrated against an α-Fe foil. The spectrum (Fig. 2) was fitted using the software *MossA* (Prescher *et al.*, 2012) with two doublets assigned to Fe^{2+}, one doublet assigned to Fe^{3+}, and one weak doublet (4.3%) assigned to $Fe^{2.5+}$ due to electron delocalisation (Table 6). This resulted in an $Fe^{3+}/\Sigma Fe_{tot}$ ratio of 0.58 (with $Fe^{2.5+}$ distributed equally on Fe^{2+} and Fe^{3+}).

Single-crystal infrared spectroscopy

Polarised Fourier-transform infrared (FTIR) absorption spectra were measured on a 44 μm thick doubly-polished single crystal section oriented parallel to the **c** axis. A Bruker Vertex 70 spectrometer attached to a Hyperion 2000 microscope was used to collect spectra in the range 2000–13000 cm^{-1} at a resolution of 4 cm^{-1}. Spectra recorded in polarised mode parallel to the crystallographic **c**-axis show an intense, off-scale band around 3550 cm^{-1}, a strong band at 3726 cm^{-1} and a weak shoulder feature at 3763 cm^{-1} (Fig. 3). As typically observed for tourmaline spectra in the (OH) range, the main band is off-scale for the **E**||**c** direction owing to excessive absorption. Spectra obtained perpendicular to the **c**-axis show considerably weaker bands, centred at 3562 and 3726 cm^{-1}. The presence of bands above 3650 cm^{-1} is worth noting; this is the region where bands due to (OH) at the O(1) (≡ W) site are expected (e.g. Gonzalez-Carreño *et al.*, 1988; Bosi *et al.*, 2015).

On the basis of studies by Bosi *et al.* (2016) and Berryman *et al.* (2016) and Watenphul *et al.* (2016), the main FTIR bands at ~3562 cm^{-1} are probably caused by the occurrence of the atomic arrangements $[^{Y}(Mg)^{Z}(Fe^{3+})^{Z}Al]$–$[^{Y}(Fe^{2+})^{Z}Al^{Z}Al]$–$[^{Y}(Fe^{3+})^{Z}Al^{Z}Al]$–$^{O(3)}(OH)_3$, whereas the band at ~3726 cm^{-1} may be caused by the arrangements $^{Y}[Mg(Mg,Fe^{2+})(Mg,Fe^{3+})]$–$^{O(1)}(OH)$–$^{X}(Na)$.

Optical absorption spectroscopy (OAS)

Polarised room-temperature optical absorption spectra in the range of 30000–11500 cm^{-1} were recorded at a spectral resolution of 1 nm on the same polished single-crystal fragment as used for FTIR measurements. We used an AVASPEC-ULS2048 ×16 spectrometer attached to a 400 μm ultraviolet (UV) optical fibre cable with a Zeiss Axiotron UV-microscope. A 75 W xenon arc lamp was used as light source, Zeiss Ultrafluar 10× lenses served as objective and condenser, and an UV-quality Glan-Thompson prism, with a working range from 40000 to 3704 cm^{-1} was used as a polariser. Spectral data in the range 10000–5000 cm^{-1} were obtained from the FTIR measurements.

The spectra show broad and strongly polarised (O > E) absorption bands at 22000, 14250 and 8790 cm^{-1}, and two additional sharper and less intense bands at 20400 and 18300 cm^{-1} (Fig. 4). In agreement with previous optical studies of tourmaline (e.g. Mattson and Rossman, 1987), the bands at 14250 and 8790 cm^{-1} are assigned to Fe^{3+}-enhanced spin-allowed *d-d* transitions in six-coordinated Fe^{2+}. The broad, intense and strongly E||O-polarised band at 22000 cm^{-1} is due to Fe^{2+} –Ti^{4+} intervalence charge-transfer processes (e.g. Smith, 1978; Taran *et al.*, 1993). The less intense bands at 20400 and 18300 cm^{-1} are caused by electronic transitions in Fe^{3+}–Fe^{3+} pairs at the Z and *Y* sites, respectively (Mattson and Rossman, 1984; Taran and Rossman, 2002).

Table 4. Powder X-ray diffraction pattern of ferro-bosiite. Only the reflections with $I \geq 5$ % are listed. The eight strongest reflections are given in bold

h	*k*	*l*	*I* (%)	d_{obs} (Å)	d_{cal} (Å)
1	**0**	**1**	**51**	**6.465**	**6.458**
0	2	1	22	5.036	5.031
0	3	0	22	4.632	4.632
2	**1**	**1**	**48**	**4.264**	**4.262**
2	**2**	**0**	**62**	**4.013**	**4.011**
0	**1**	**2**	**46**	**3.529**	**3.527**
1	3	1	8	3.407	**3.408**
1	4	0	8	3.033	3.032
1	**2**	**2**	**59**	**2.998**	2.996
3	2	1	7	2.923	2.921
3	1	2	6	2.648	2.649
0	**5**	**1**	**100**	**2.597**	**2.597**
0	0	3	6	2.433	2.431
2	3	2	17	2.401	2.400
5	1	1	14	2.362	2.361
5	0	2	17	2.211	2.210
4	3	1	6	2.181	2.180
3	0	3	6	2.154	2.153
4	2	2	6	2.132	2.131
2	2	3	9	2.080	2.079
1	**5**	**2**	**41**	**2.059**	**2.060**
1	6	1	7	2.036	2.035
3	**4**	**2**	**23**	**1.937**	**1.936**
1	4	3	7	1.898	1.897
6	2	1	6	1.864	1.863
0	6	3	19	1.678	1.677
2	7	1	12	1.654	1.653
5	5	0	15	1.605	1.605
7	2	2	5	1.540	1.539
0	5	4	14	1.525	1.525
5	1	4	22	1.473	1.472
4	7	0	5	1.441	1.441
6	5	1	7	1.429	1.428
4	3	4	9	1.426	1.425
6	3	3	5	1.421	1.421
10	0	1	8	1.365	1.365
10	1	0	8	1.319	1.319
5	0	5	10	1.292	1.298
10	1	3	5	1.160	1.159

Determination of number of atoms per formula unit (apfu)

In agreement with the structure-refinement results, the boron content was assumed to be stoichiometric (B^{3+} = 3.00 apfu). The iron oxidation state was determined by Mössbauer spectroscopy. In accordance with these results and Fe and Mn redox potential arguments, all Mn was considered as Mn^{2+}. The Li content was determined by μ-LIBS. The presence of (OH) was demonstrated by FTIR. The amounts of (OH) and the formula were then calculated by charge balance with the assumption T + Y + Z = 15.00 apfu and 31 anions. The excellent agreement between the number of electrons per formula unit (epfu) derived from EMPA and SREF (272.0 and 272.2 epfu, respectively) supports the assumptions regarding stoichiometry.

Site populations

The ferro-bosiite site populations at the *X*, *B*, *T*, O3 (≡ V) and O1 (≡ W) sites follow the standard site preference suggested for tourmaline (e.g. Henry *et al.*, 2011) and are coherent with the information from FTIR absorption spectra (Fig. 3). The cation distribution at the *Y* and *Z* sites was optimised according to the procedure of Bosi *et al.* (2017) and Wright *et al.* (2000), and by fixing the minor elements Ti^{4+}, V^{3+}, Mn^{2+} and Li at the *Y* site. The resulting empirical crystal-chemical formula is:

Table 5. Chemical data (wt.%) and atoms per formula unit (apfu) normalised to 31 anions for ferro-bosiite

Constituent	Mean (6 spots)	Range	apfu
SiO_2	33.54(24)	33.15–33.77	5.994
TiO_2	1.21(34)	0.85–1.78	0.163
B_2O_3*	9.73		3.000
Al_2O_3	20.55(83)	18.92–21.25	4.328
V_2O_3	0.11(3)	0.07–0.16	0.016
Fe_2O_3[b]	14.62		1.966
FeO[b]	9.49		1.418
MnO	0.21(5)	0.14–0.29	0.032
MgO	3.98(19)	3.75–4.28	1.060
Li_2O[c]	0.033(5)	0.027–0.035	0.024
Na_2O	2.87(3)	2.84–2.92	0.993
K_2O	0.09(2)	0.06–0.12	0.020
F	0.08(7)	0.02–0.22	0.044
H_2O[a]	2.81		3.344
O = F	−0.03		
Total	99.28		
FeO_{tot}	22.64(51)	22.20–23.60	

Notes: Errors for oxides and fluorine are standard deviations (in parentheses).
[a]Calculated by stoichiometry, (Y+Z+T) = 15.00 apfu.
[b]Determined by Mössbauer spectroscopy.
[c]Determined by μ-Laser Induced Breakdown Spectroscopy.

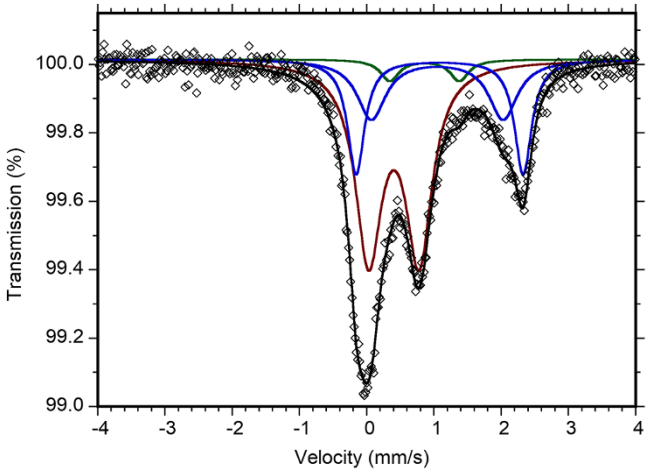

Figure 2. Mössbauer spectrum of ferro-bosiite. The fitted absorption doublets assigned to Fe^{2+} are indicated in blue, Fe^{3+} in red, and $Fe^{2.5+}$ due to electron delocalisation in green. Diamonds denote the measured spectrum, and the black curve represents the summed fitted spectrum.

Table 6. Mössbauer parameters for ferro-bosiite obtained at room-temperature

δ (mm/s)	ΔE_Q (mm/s)	FWHM (mm/s)	*I* (%)	Assignment
1.08	2.48	0.30	21.3	$^{[6]}Fe^{2+}$
1.05	1.96	0.51	18.5	$^{[6]}Fe^{2+}$
0.86	1.03	0.33	4.3	$^{[6]}Fe^{2.5+}$
0.40	0.75	0.47	55.9	$^{[6]}Fe^{3+}$

δ = centroid shift, ΔE_Q = quadrupole splitting, FWHM = full width at half-maximum.

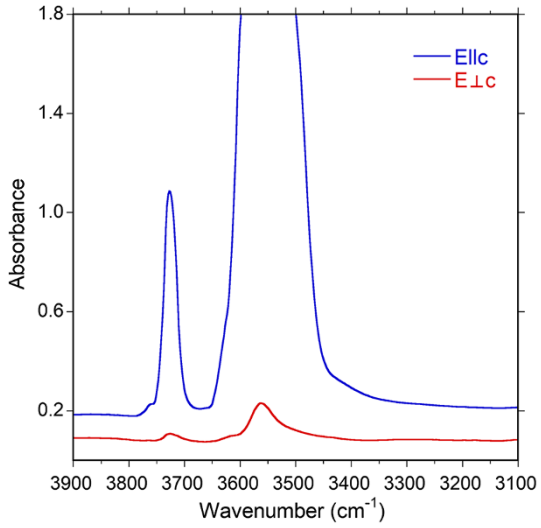

Figure 3. Polarised FTIR spectra of ferro-bosiite. Note the presence of bands above 3650 cm^{-1}. The main band is truncated around two absorbance units in the **E**||**c** direction owing to excessive absorption.

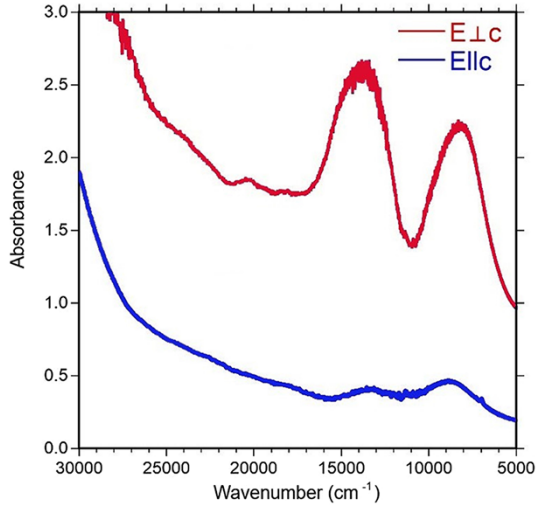

Figure 4. Polarised optical absorption spectra of ferro-bosiite in the UV-VIS-NIR region.

$^{X}(Na_{0.99}K_{0.02})_{\Sigma 1.01}\,^{Y}(Fe^{3+}_{1.56}V^{3+}_{0.02}Mg_{1.01}Fe^{2+}_{0.20}Mn^{2+}_{0.03}Ti_{0.16}Li_{0.02})_{\Sigma 3.00}\,^{Z}(Al_{4.32}Fe^{3+}_{0.41}Fe^{2+}_{1.22}Mg_{0.05})_{\Sigma 6.00}\,^{T}[(Si_{5.99}Al_{0.01})_{\Sigma 6.00}O_{18}](BO_3)_3\,^{O(3)}(OH)_3\,^{O(1)}[O_{0.62}(OH)_{0.34}F_{0.04}]_{\Sigma 1.00}$.

The observed site-scattering values, expressed as the number of electrons per site, and the mean bond lengths, alongside those calculated from the empirical formula are presented in Table 7. The excellent agreement between the observed and calculated values, coupled with the results from bond-valence optimisation, strongly supports the distribution of cations over the *X*, *Y*, *Z*, and *T* sites in ferro-bosiite, as well as the comparison of weighted bond-valence sums, and the weighted atom valence (also referred to as the mean formal charge), calculated from the empirical formula (Table 8). Supplementary Figs S3 and S4 shows that the absence of ^{Y}Al in the present sample (with Al solely at *Z*) is consistent with the negative correlation between ^{Y}Al and the value of the Z–O7D bond length (the longer of the two Z–O7 distances in the tourmaline structure), as well as of the unit-cell *a*-parameter, as proposed by Bosi and Lucchesi (2007) and Bosi *et al.* (2010).

Table 7. Observed site-scattering values, in terms of number of electrons per site (eps) and mean bond-lengths (mdl, in Å) compared to calculated ones from the optimised site-populations for ferro-bosiite

		eps		mdl	
	Site population (apfu[a])	Obs.	Calc.	Obs.	Calc.[b]
X =	0.99 Na + 0.02 K	11.06(14)	11.31	2.709	2.710[c]
Y =	1.56 Fe^{3+} + 0.02 V + 1.01 Mg + 0.20 Fe^{2+} + 0.03 Mn + 0.16 Ti + 0.02 Li	20.89(13)	20.84	2.042	2.042
Z =	4.32 Al + 0.41 Fe^{3+} + 1.22 Fe^{2+} + 0.05 Mg	16.58(8)	16.53	1.957	1.956
T =	5.99 Si + 0.01 Al	14[d]	14	1.619	1.619

[a]Atoms per formula unit.
[b]From empirical ionic radii reported in Bosi and Lucchesi (2007).
[c]In accord with the *X* site population (= 1.00 Na + 0.02 K) observed for oxy-chromium-dravite (Bosi *et al.*, 2012).
[d]Fixed in the final stages of refinement.

Table 8. Weighted bond valences (in valence units) and bond valence sums (BVS) for ferro-bosiite compared to expected values (mean formal charge, MFC) calculated from the empirical formula

Site	*X*	*Y*	*Z*	*T*	*B*	Σ_{anions}
O(1)		$0.48^{\times 3\rightarrow}$				1.45
O(2)	$0.16^{\downarrow \times 3}$	$0.45^{\times 2\downarrow \rightarrow}$			1.01	2.06
O(3)		0.33	$0.41^{\times 2\rightarrow}$			1.16
O(4)	$0.07^{\downarrow \times 3}$			$0.99^{\times 2\rightarrow}$		2.05
O(5)	$0.08^{\downarrow \times 3}$			$0.96^{\times 2\rightarrow}$		2.00
O(6)		$0.45^{\downarrow \times 2}$	0.50	1.05		2.00
O(7)			0.49	1.05		1.97
			0.42			
O(8)			0.46		$1.00^{\downarrow \times 2}$	1.97
			0.50			
BVS	0.90	2.61	2.79	4.05	3.02	
MFC	1.01	2.62	2.79	4.00	3.00	

Notes: Weighted bond valence according to Bosi (2014). Bond valence parameters from Brown and Altermatt (1985).

End-member formula and relation to other species

From the above empirical formula, the composition of the present sample is consistent with an oxy-tourmaline belonging to the alkali group (Henry *et al.*, 2011), with Na dominant at the *X* position (see the ternary compositional plots below) and 'oxy-group' (O^{2-}) dominant at the O(1) (≡ W) site; the dominant constituent at *Y* is Fe^{3+}. With regard to the *Z* position, the formula electroneutrality requires that the total charge at *Z* is +16 in the end-member formula: $NaFe^{3+}{}_3(Z_6)^{\Sigma 16+}(Si_6O_{18})(BO_3)_3(OH)_3O$. In accord with the dominant-valency rule and the valency-imposed double site-occupancy (Hatert and Burke, 2008), the unique possible charge-arrangement compatible with the *Z*-site population is $^{Z}(3^{+}{}_4 2^{+}{}_2)^{\Sigma 16+}$. As Fe^{2+} and Al^{3+} prevail among the 2^+ and 3^+ cations at the *Z* sites, the atomic arrangement $(Al^{3+}{}_4Fe^{2+}{}_2)$ is the dominant one. The end-member composition may hence be represented as $NaFe^{3+}{}_3(Al_4Fe^{2+}{}_2)(Si_6O_{18})(BO_3)_3(OH)_3O$. As no tourmaline is currently approved with this composition, it can be identified as a new species.

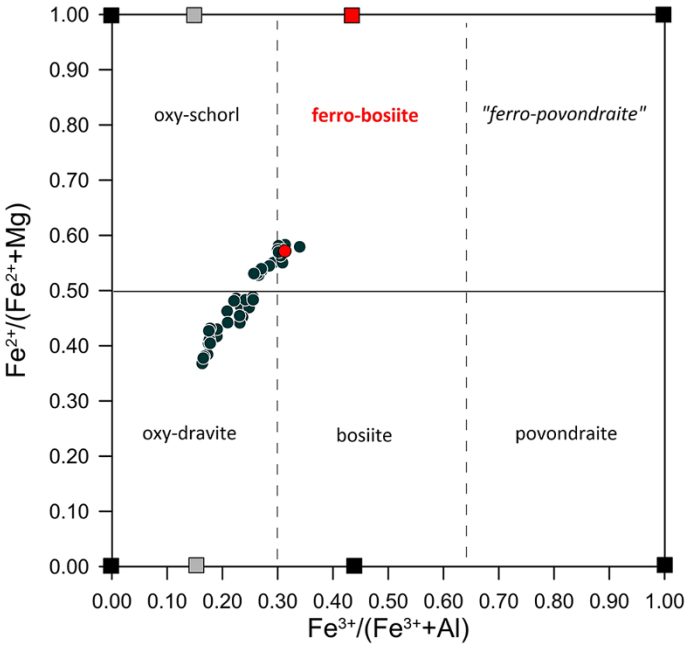

Figure 5. Plot of $Fe^{2+}/(Fe^{2+}+Mg)$ *versus* $Fe^{3+}/(Fe^{3+}+Al)$ showing the compositional trend of our tourmalines towards ferro-bosiite, $NaFe^{3+}{}_3(Al_4Fe^{2+}{}_2)(Si_6O_{18})(BO_3)_3(OH)_3O$ (red square), rather than toward hypothetical Fe^{3+}-analogues of oxy-schorl $Na(Fe^{2+}{}_2Fe^{3+})Al_6(Si_6O_{18})(BO_3)_3(OH)_3O$ (grey square at the top of the plot); the grey square at the bottom of the plot refers to the hypothetical Fe^{3+}-analogues of oxy-dravite. This diagram is also useful for establishing the appropriate tourmaline oxy-species within the alkali group. It can be interpreted as reflecting the combined chemical composition of the *Y* and *Z* sites: $^{Y+Z}(Al_{4.32}Fe^{3+}{}_{1.97}Fe^{2+}{}_{1.42}Mg_{1.06}Ti_{0.16}Mn^{2+}{}_{0.03}V^{3+}{}_{0.02}Li_{0.02})_{\Sigma 9.00}$. Thus, disregarding the actual (or ordered) distribution of cations over these two sites, the constituents that define the dominant end-member composition are Al, Fe^{3+} and Fe^{2+} in a ratio of 4:3:2. This is consistent with the arrangement $[^{Y}(Fe^{3+}{}_3)\ {}^{Z}(Al_4Fe^{2+}{}_2)]$. Data from the type locality are single spot analyses (= 41) on the several fragments from the acicular black tourmalines of the overgrowth sector containing holotype (dark-green circle) and the average value of the holotype fragment used for SREF (red circle). Black squares represent ideal composition for: oxy-schorl $Na(Fe^{2+}{}_2Al)(Al_6)(Si_6O_{18})(BO_3)_3(OH)_3O$; oxy-dravite $Na(Al_2Mg)(Al_5Mg)(Si_6O_{18})(BO_3)_3(OH)_3O$; bosiite $NaFe^{3+}{}_3(Al_4Mg_2)(Si_6O_{18})(BO_3)_3(OH)_3O$; povondraite $Na(Fe^{3+}{}_3)(Fe^{3+}{}_4Mg_2)(Si_6O_{18})(BO_3)_3(OH)_3O$; hypothetical 'ferro-povondraite' $Na(Fe^{3+}{}_3)(Fe^{3+}{}_4Fe^{2+}{}_2)(Si_6O_{18})(BO_3)_3(OH)_3O$.

Table 9. Comparative data for ferro-bosiite, bosiite, oxy-dravite and oxy-schorl

	Ferro-bosiite[a]	Bosiite[b]	Oxy-dravite[c]	Oxy-schorl[d]
a (Å)	16.0499(5)	16.101(3)	15.9273(2)	15.916(3)
c	7.2977(2)	7.327(2)	7.2001(1)	7.107(1)
V (Å^3)	1628.03(11)	1645.0(6)	1581.81(4)	1559.1(4)
Space group	*R*3*m*	*R*3*m*	*R*3*m*	*R*3*m*
Optic sign	Uniaxial (–)	Uniaxial (–)	Uniaxial (–)	Uniaxial (–)
ω	1.675(5)	1.760(5)	1.650(5)	1.663(2)
ε	1.645(5)	1.687(5)	1.620(5)	1.641(2)
Streak	Brown	Pale brown	Pink	Pale grey
Colour	Black	Dark brown to black	Dark red	Greenish black
Pleochroism	O = dark grey	O = yellow-brown	O = orange	O = green to bluish green
	E = pale yellow	E = red-brown	E = pink	E = pale yellowish to nearly colourless
Strong lines in the powder	2.598 (100)	2.606 (100)	2.963 (100)	2.569 (100)
XRD pattern *d*(Å) (*I*, %)	4.012 (62)	8.051 (58)	3.438 (84)	2.934 (59)
	2.997 (59)	3.008 (58)	2.576 (68)	1.910 (54)
	6.461 (51)	4.025 (57)	4.222 (67)	3.977 (53)
	4.264 (48)	3.543 (50)	3.983 (64)	3.439 (53)
	3.529 (46)	4.279 (46)	1.915 (52)	1.591 (48)
	2.060 (41)	2.068 (45)	6.377 (44)	2.030 (41)
Reference	This work	Ertl *et al.* (2016)	Bosi and Skogby (2013)	Bačík *et al.* (2013)

Notes – formulae:
[a]= $NaFe^{3+}{}_3(Al_4Fe^{2+}{}_2)(Si_6O_{18})(BO_3)_3(OH)_3O$
[b]= $NaFe^{3+}{}_3(Al_4Mg_2)(Si_6O_{18})(BO_3)_3(OH)_3O$
[c]= $Na(Al_2Mg)(Al_5Mg)(Si_6O_{18})(BO_3)_3(OH)_3O$
[d]= $Na(Fe^{2+}{}_2Al)Al_6(Si_6O_{18})(BO_3)_3(OH)_3O$

Note that the so-called ordered formula (i.e. that with 3^+-cations ordered at Z and the remainder at Y) usually required for classification purposes (Henry *et al.*, 2011) is:

$^{X}(Na_{0.99}K_{0.02})_{\Sigma 1.01}{}^{Y}(Fe^{3+}{}_{0.31}Mg_{1.06}Fe^{2+}{}_{1.42}Mn^{2+}{}_{0.03}Ti_{0.16}Li_{0.02})_{\Sigma 3.00}{}^{Z}(Al_{4.32}V^{3+}{}_{0.02}Fe^{3+}{}_{1.66})_{\Sigma 6.00}{}^{T}[(Si_{5.99}Al_{0.01})_{\Sigma 6.00}O_{18}](BO_3)_3{}^{V}(OH)_3{}^{W}[O_{0.62}(OH)_{0.34}F_{0.04}]_{\Sigma 1.00}$.

This formula would lead to the end-member $Na(Fe^{2+}{}_2Fe^{3+})Al_6(Si_6O_{18})(BO_3)_3(OH)_3O$, which is the Fe^{3+}analogue of oxy-schorl, which is at odds with the compositional variation in tourmalines of the black overgrowth in this study as shown by the nomenclature diagram in Fig. 5. All this follows Henry *et al.* (2013): "*For the purposes of classification of tourmaline species, actual tourmaline structural information of the Y- and Z-site occupancy is an overriding consideration for the definition of a tourmaline species*".

The name ferro-bosiite, $NaFe^{3+}{}_3(Al_4Fe^{2+}{}_2)(Si_6O_{18})(BO_3)_3(OH)_3O$, is proposed for that chemical composition, following Henry *et al.* (2011). The prefix *ferro* expresses the substitution of $2Fe^{2+}$ for 2Mg in the root composition of bosiite, $NaFe^{3+}{}_3(Al_4Mg_2)(Si_6O_{18})(BO_3)_3(OH)_3O$ (Fig. 5). The proposed

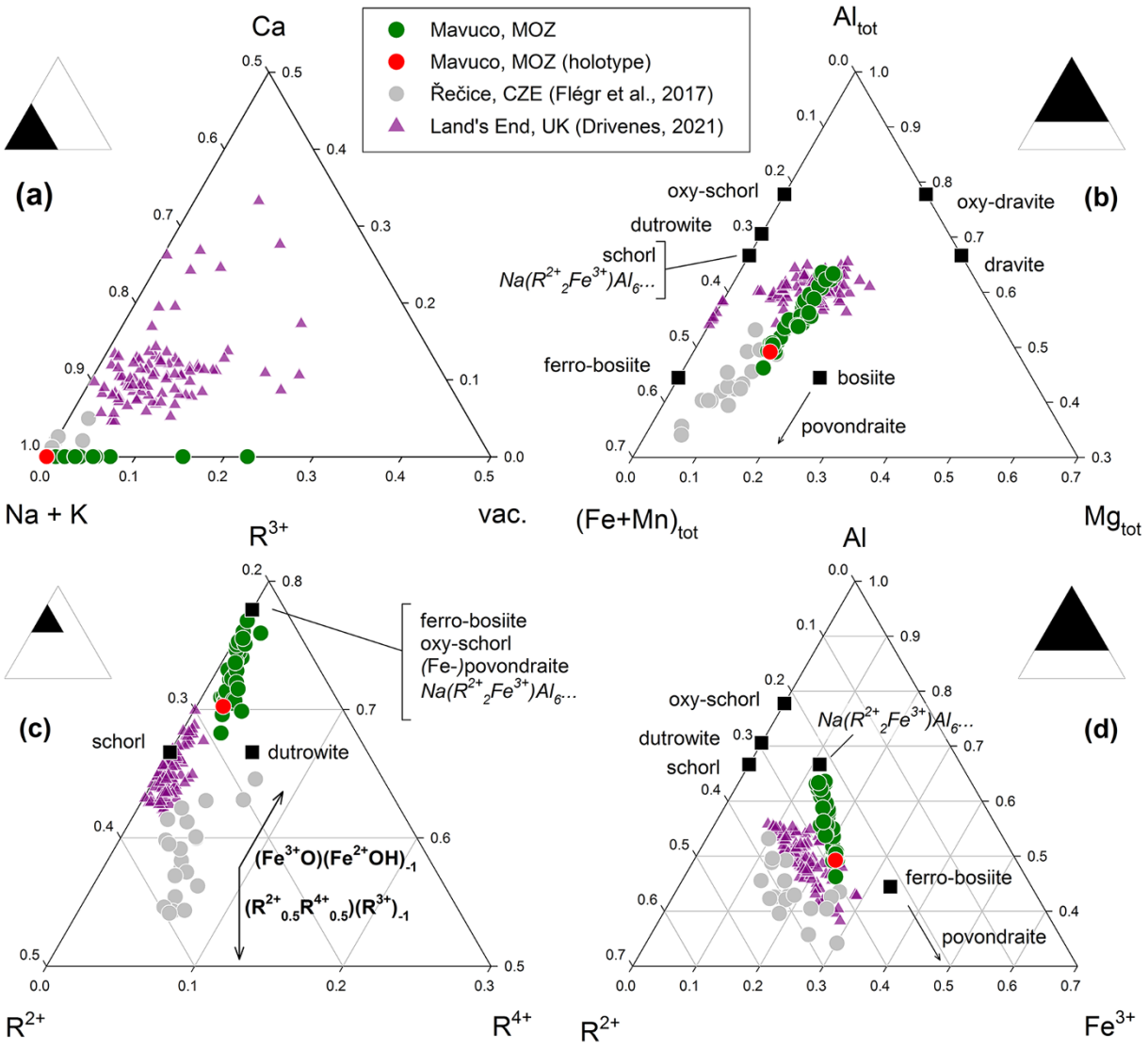

Figure 6. Ternary compositional plots comparing ferro-bosiite from the type locality with published tourmaline compositions. (a) *X*-site occupancy; (b) ratios of octahedrally coordinated Mg_{tot} *versus* Al_{tot} *versus* $(Fe+Mn)_{tot}$; (c) ratios of octahedrally coordinated cations R^{4+} *versus* R^{3+} *versus* R^{2+}; (d) ratios of octahedrally coordinated cations Fe^{3+} *versus* Al^{3+} *versus* R^{2+}. Black squares show ideal end-member compositions.

name ferro-bosiite adheres to the general guidelines for the nomenclature of tourmalines and does not violate the rule that prohibits naming a mineral after oneself. In accordance with Warr (2021), Fbos represents the symbol for ferro-bosiite.

Ferro-bosiite belongs to alkali-subgroup 3 of the tourmaline supergroup (Henry *et al.*, 2011). It is closely related to bosiite by the exchange $(^{Z}Fe^{2+})(^{Z}Mg)_{-1}$, and to povondraite by the combination of exchanges $(^{Z}Fe^{2+}{}_2{}^{Z}Al_4)(^{Z}Mg_2{}^{Z}Fe^{3+}{}_4)_{-1}$. In addition to being the Fe^{2+} analogue of bosiite and Fe^{3+} analogue of hypothetical 'ferro-povondraite', ferro-bosiite is also the Fe^{3+} analogue of oxy-schorl (Bačík *et al.*, 2013) through the exchange $(Fe^{3+})_3(Al)_{-3}$, which is the result of the more complex exchange $(^{Y}Fe^{3+}{}_3{}^{Z}Fe^{2+}{}_2)(^{Y}Fe^{2+}{}_2{}^{Y}Al^{Z}Al_2)_{-1}$. Similarly, the relation to oxy-dravite (Bosi and Skogby, 2013) may be described by the exchange $(^{Y}Fe^{3+}{}_3{}^{Z}Fe^{2+}{}_2)(^{Y}Mg^{Y}Al_2{}^{Y}Mg\ {}^{Z}Al)_{-1}$. In other words, the position of ferro-bosiite within the tourmaline supergroup reflects subtle compositional variations, mainly in Fe^{2+}, Fe^{3+}, Mg and Al, that distinguish it from closely related species.

The properties of ferro-bosiite, bosiite, oxy-dravite and oxy-schorl are compared in Table 9.

Ferro-bosiite solid solutions

The concentrations of main elements in tourmaline associated with ferro-bosiite from the Marina pegmatite show a gradual variation in the proportions of Mg_{tot}, Al_{tot} and Fe_{tot}, $Fe^{3+}/(Al+Fe^{3+})$ and in the ratios $Mg/(Fe^{2+}+Mg)$, as well as in Ti contents and, to a lesser extent, in the $^{X}\square$ amounts (Figs 6 and 7). At the Fe^{3+}-poor, Mg-rich end of the geochemical trend, compositions probably correspond to the hypothetical Fe^{3+} analogue of oxy-dravite. In contrast, the Fe^{3+}-rich compositions are dominated by ferro-bosiite with a progressively increasing involvement of the dutrowite component, ideally $Na(Fe^{2+}{}_{2.5}Ti_{0.5})Al_6(Si_6O_{18})(BO_3)_3(OH)_3O$ (Figs 6c,d and 7b). The tourmalines of the black overgrowth in this study may be represented by the evolution Fe^{3+}-rich oxy-dravite → Fe^{3+}-rich oxy-schorl → ferro-bosiite → Fe^{3+}-rich dutrowite, in which the

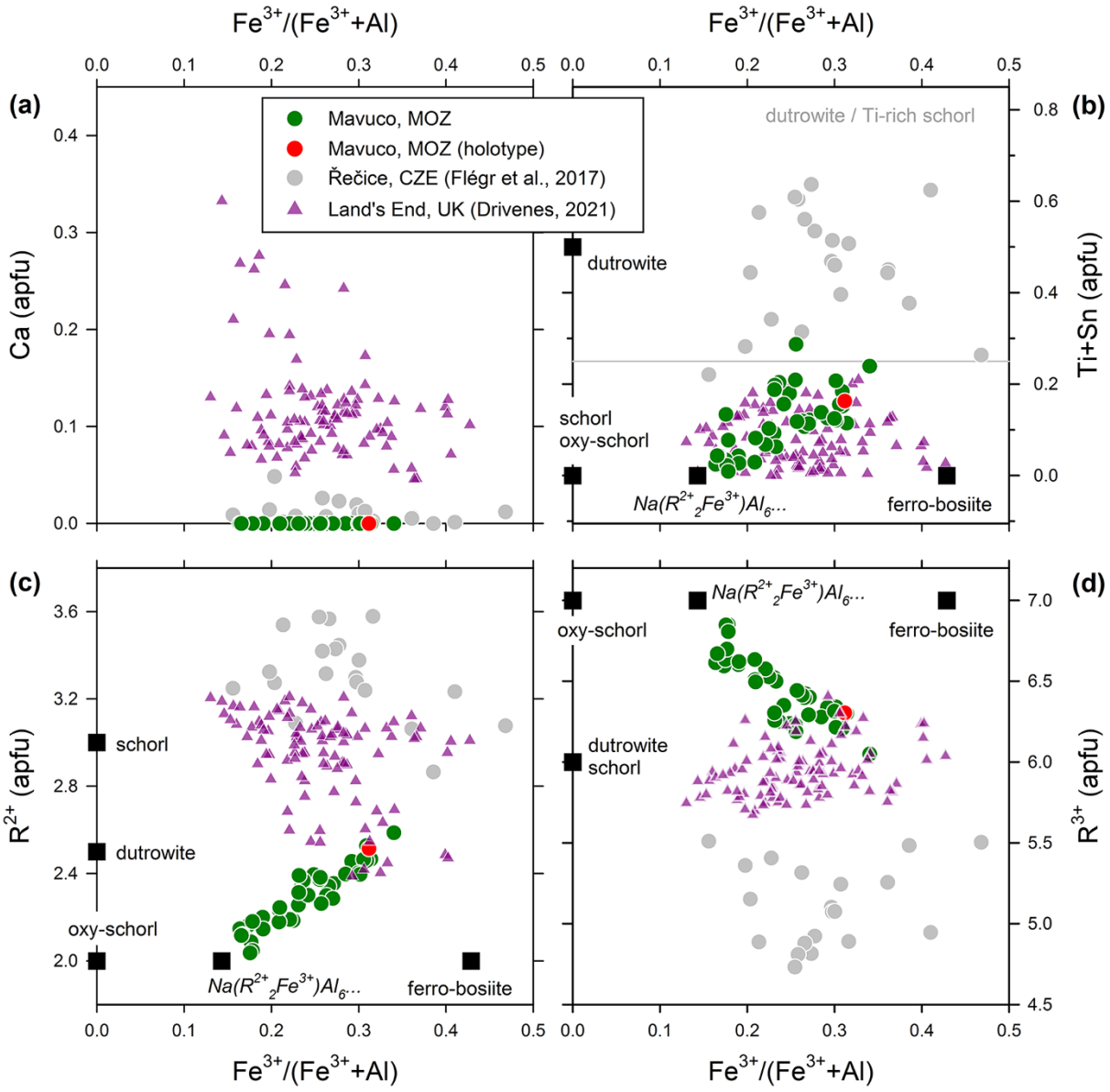

Figure 7. Binary compositional plots comparing ferro-bosiite from the type locality with published tourmaline compositions. (a) Plot of $Fe^{3+}/(Fe^{3+}+Al)$ *versus* Ca; (b) plot of $Fe^{3+}/(Fe^{3+}+Al)$ *versus* Ti+Sn; (c) plot of $Fe^{3+}/(Fe^{3+}+Al)$ *versus* octahedrally coordinated divalent cations R^{2+}; (d) plot of $Fe^{3+}/(Fe^{3+}+Al)$ *versus* octahedrally coordinated divalent cations R^{3+}.

occurrence of a minor bosiite component cannot be excluded (Figs 5, 6, and 7).

In the commonly used Mg_{tot}–Al_{tot}–Fe_{tot} compositional diagram, the ferro-bosiite data partially overlap with some earlier published Na-dominant compositions (Fig. 6b). However, their classification is strongly influenced by the Fe^{3+}/Fe_{tot} ratio and the Ti contents, as both parameters significantly affect the overall charge and incorporation of the O^{2-} in place of (OH) and F.

Flégr *et al.* (2017) described tourmaline with a composition close to that of ferro-bosiite from the Řečice pegmatite. This tourmaline is characterised by ^{X}Na dominance (Fig. 6a), strong Al depletion relative to schorl (Fig. 6b), very high Ti contents (up to 0.6 apfu) and a Fe^{3+}/Fe_{tot} ratio of ~0.25–0.45 (unpublished data, JC). Although its Mg_{tot}–Al_{tot}–Fe_{tot} proportions are consistent with those of bosiite or ferro-bosiite, the proportion of di-, tri-, and tetravalent octahedrally coordinated cations indicate the presence of a dutrowite component (Fig. 6c). At the same time, the overall content of trivalent cations (and thus ^{W}O) is too low to satisfy the requirements for classification as dutrowite or ferro-bosiite (Figs 5, 7c and 7d). Consequently, the Řečice tourmaline should be classified as Ti-rich schorl. A compositionally and texturally similar tourmaline was reported by Pieczka and Sęk (2017) from the Juliana pegmatite, SW Poland. In both occurrences, the tourmaline formed through metasomatic replacement of biotite. A rather unique Na-dominant tourmaline compositionally close to ferro-bosiite has been described by Drivenes (2022; Fig. 7a,b). This tourmaline exhibits strong zoning, with an Fe-rich outermost fibrous rims (zone 5) characterised by elevated Sn^{4+} (up to 0.184 apfu) and Ca (up to 0.378 apfu). However, its Fe^{3+}/Fe_{tot} ratio could not be determined, and calculation of the minimum Fe^{3+} required for charge balance [assuming 4 (OH+F) apfu] results in its classification as schorl (Fig. 7c,d).

It is important to emphasise that the accurate classification of the tourmalines mentioned above depends on the determination of the Fe^{3+}/Fe_{tot} ratio. In all cases except the holotype material, the crystals are too chemically heterogeneous to allow the acquisition of meaningful spot Mössbauer spectra or single-crystal X-ray diffraction data. Some of the published compositions may correspond to ferro-bosiite if they contain sufficient $^{W}O^{2-}$, that is, if their Fe^{3+} content is sufficiently high. In general, an Fe-rich tourmaline of ferro-bosiite composition is characterised by a significant dutrowite component (or its Sn-analogue) and by a dominant contribution from the $[(Fe^{2+},Mg)Ti^{4+}][(Al,Fe^{3+})_2]_{-1}$ vector, or generally, the $(R^{2+} + Ti^{4+}) = 2R^{3+}$ exchange mechanism (Fig. 6c). In the Mavuco tourmaline, the decrease of R^{3+} along with increase of the $Fe^{3+}/(Fe^{3+}+Al)$ and $Fe^{2+}/(Fe^{2+}+Mg)$ ratios (Figs 7d and 5) and Ti contents (Fig. 7b) indicates that the exchange clearly involves Al over Fe^{3+} and Fe^{2+} over Mg, i.e. the $Fe^{2+}Ti^{4+}Al_{-2}$ exchange prevails. On the other hand, these trends are not distinct in data from the two other localities.

Genetic inferences of ferro-bosiite

The Marina pegmatite, where ferro-bosiite was discovered, is part of a poorly documented gem-bearing pegmatite field hosted in Pan-African metasedimentary and migmatitic units in the Mavuco area (Alto Ligonha, Mozambique; Macey *et al.*, 2006). Ferro-bosiite crystallised as a 3–4 mm thick overgrowth on a large, previously formed, multicoloured elbaitic–liddicoatitic tourmaline crystal, following a major pocket collapse. This collapse affected not only the crystals of the various minerals present at the roof of the pocket but also the rocks of the intermediate and border zones, and even the surrounding amphibolite country rock in which the evolved magma intruded. Such large-scale collapses are reminiscent of those described in the so-called 'chamber pegmatites' of Volodarsk-Volynskii, Ukraine (Lyckberg *et al.*, 2009).

Ferro-bosiite occurs along basal fracture surfaces of primary elbaitic–liddicoatitic crystals. However, the late-stage hydrothermal tourmaline found on fractures and external surfaces of these crystals exhibits two distinct compositions: ferro-bosiite forms overgrowths along the direction of the analogous pole, whereas dravitic and schorlitic tourmalines develop on other crystal faces and breakage surfaces. This compositional variation in the overgrowth along different crystallographic directions is a result of hourglass zoning, a type of sector zoning in which crystal sectors develop significantly different compositions depending on their growth direction (van Hinsberg *et al.*, 2006).

This complex overgrowth sequence on the early Li-rich tourmaline, ranging from oxy-dravite and oxy-schorl to ferro-bosiite and dutrowite, reflects a sudden change in the geochemical conditions within the cavity, marked by a sharp increase in Fe and Mg concentrations in the late-stage fluids. These elements were probably derived from the breakdown of amphibolitic wallrock, exposed in the pocket during the collapse and subsequently altered by the action of aggressive late-stage fluids. Similar mechanisms, where pegmatitic cavity fluids interact with primitive minerals in the border zone of the pegmatite or with minerals in the host rock, have been documented in previous studies by Altieri *et al.* (2022, 2023). These interactions often lead to Fe-rich transitions, and in some cases, involve elements such as Mn, Ti and Mg.

Supplementary material. The supplementary material for this article can be found at at https://doi.org/10.1180/mgm.2025.10114.

Acknowledgements. Chemical analyses were done with the kind assistance of M. Serracino to whom the authors express their gratitude. F.B. acknowledges funding by Sapienza University of Rome (Prog. Università 2023) and by the Italian Ministry of Education (MIUR)–PRIN 2020, ref. 2020WYL4NY. J.C. acknowledges funding from project GAČR 19-17276S. We sincerely appreciate the valuable comments provided by reviewers Andreas Ertl, Darrell J. Henry and Adam Pieczka, as well as by Structures Editor Peter Leverett and Guest Editor Robert F. Martin. This paper is dedicated to Edward Sturgis Grew, whose enduring passion for boron minerals has been a source of inspiration for the mineralogical community.

Competing interests. The authors declare none.

References

Altieri A., Pezzotta F., Skogby H., Hålenius U. and Bosi F. (2022) Blue-growth zones caused by Fe^{2+} in tourmaline crystals from the San Piero in Campo gem-bearing pegmatites, Elba Island, Italy. *Mineralogical Magazine*, **86**, 910–919.

Altieri A., Pezzotta F., Skogby H., Hålenius U. and Bosi F. (2023) Dark-coloured Mn-rich overgrowths in an elbaitic tourmaline crystal from the Rosina pegmatite, San Piero in Campo, Elba Island, Italy: witness of late-stage opening of the geochemical system. *Mineralogical Magazine*, **87**, 130–142.

Bačík P. and Fridrichová G. (2021) Cation partitioning among crystallographic sites based on bond-length constraints in tourmaline-supergroup minerals. *American Mineralogist*, **106**, 851–861.

Bačík P., Cempírek J., Uher P., Novák M., Ozdín D., Filip J., Škoda R., Breiter K., Klementová M. and Ďuďa R. (2013) Oxy-schorl, $Na(Fe_2^{2+}Al)Al_6Si_6O_{18}(BO_3)_3(OH)_3O$, a new mineral from Zlatá Idka, Slovak Republic and Přibyslavice, Czech Republic. *American Mineralogist*, **98**, 485–492.

Berryman E.J., Wunder B., Ertl A., Koch-Müller M., Rhede D., Scheidl K., Giester G. and Heinrich W. (2016) Influence of the X-site composition on tourmaline's crystal structure: Investigation of synthetic K-dravite, dravite, oxy-uvite, and magnesio-foitite using SREF and Raman spectroscopy. *Physics and Chemistry of Minerals*, **43**, 83–102.

Bosi F. (2014) Bond valence at mixed occupancy sites. I. Regular polyhedra. *Acta Crystallographica*, **B70**, 864–870.

Bosi F. and Lucchesi S. (2007) Crystal chemical relationships in the tourmaline group: structural constraints on chemical variability. *American Mineralogist*, **92**, 1054–1063.

Bosi F. and Skogby H. (2013) Oxy-dravite, $Na(Al_2Mg)(Al_5Mg)(Si_6O_{18})(BO_3)_3(OH)_3O$, a new mineral species of the tourmaline supergroup. *American Mineralogist*, **98**, 1442–1448.

Bosi F., Balić-Žunić T. and Surour A.A. (2010) Crystal structure analysis of four tourmalines from the Cleopatra's Mines (Egypt) and Jabal Zalm (Saudi Arabia), and the role of Al in the tourmaline group. *American Mineralogist*, **95**, 510–518.

Bosi F., Reznitskii L. and Skogby H. (2012) Oxy-chromium-dravite, $NaCr_3(Cr_4Mg_2)(Si_6O_{18})(BO_3)_3(OH)_3O$, a new mineral species of the tourmaline supergroup. *American Mineralogist*, **97**, 2024–2030.

Bosi F., Skogby H., Lazor P. and Reznitskii L. (2015) Atomic arrangements around the O3 site in Al- and Cr-rich oxy-tourmalines: a combined EMP, SREF, FTIR and Raman study. *Physics and Chemistry of Minerals*, **42**, 441–453.

Bosi F., Skogby H. and Balić-Žunić T. (2016) Thermal stability of extended clusters in dravite: a combined EMP, SREF and FTIR study. *Physics and Chemistry of Minerals*, **43**, 395–407.

Bosi F., Reznitskii L., Hålenius U. and Skogby H. (2017) Crystal chemistry of Al–V–Cr oxy-tourmalines from Sludyanka complex, Lake Baikal, Russia. *European Journal of Mineralogy*, **29**, 457–472.

Bosi F., Celata B., Skogby H., Hålenius U., Tempesta G., Ciriotti M.E., Bittarello E. and Marengo A. (2021) Mn-bearing purplish-red tourmaline from the Anjanabonoina pegmatite, Madagascar. *Mineralogical Magazine*, **85**, 242–253.

Bosi F., Altieri A., Skobgy H., Pezzotta F., Hålenius U., Tempesta G., Ballirano P., Flégr T. and Cempírek, J. (2023) Ferro-bosiite, IMA 2022-069. CNMNC Newsletter 70. *Mineralogical Magazine*, **87**, https://doi.org/10.1180/mgm.2022.135

Brown I.D. and Altermatt D. (1985) Bond-valence parameters obtained from a systematic analysis of the Inorganic Crystal Structure Database. *Acta Crystallographica*, **B41**, 244–247.

Bruker AXS (2016) *Topas V.6: General Profile and Structure Analysis Software for Powder Diffraction Data*. Bruker AXS, Karlsruhe, Germany.

Cheary R.W. and Coelho A. (1992) A fundamental parameters approach to X-ray line-profile fitting. *Journal of Applied Crystallography*, **25**, 109–121.

Drivenes K. (2022) Sn-rich tourmaline from the Land's End granite, SW England. *Journal of Geosciences*, **67**, 173–189.

Ertl A., Baksheev I.A., Giester G., Lengauer C.L., Prokofiev V.Yu. and Zorina L.D. (2016) Bosiite, $NaFe^{3+}{}_3(Al_4Mg_2)(Si_6O_{18})(BO_3)_3(OH)_3O$, a new ferric member of the tourmaline supergroup from the Darasun gold deposit, Transbaikalia, Russia. *European Journal of Mineralogy*, **28**, 581–591.

Flégr T., Cempírek J., Novák M. and Filip J. (2017) Ti-rich schorl to bosiite (?) from the Řečice elbaite-subtype pegmatite. Pp. 35–37 in: *Tourmaline 2017 International Symposium, Book of Abstracts*.

Gonzales-Carreño T., Fernández M. and Sanz J. (1988) Infrared and electron microprobe analysis of tourmaline. *Physics and Chemistry of Minerals*, **15**, 452–460.

Hatert F. and Burke E.A.J. (2008) The IMA–CNMNC dominant-constituent rule revisited and extended. *The Canadian Mineralogist*, **46**, 717–728.

Hawthorne F.C. and Henry D. (1999) Classification of the minerals of the tourmaline group. *European Journal of Mineralogy*, **11**, 201–215.

Henry D.J., Novák M., Hawthorne F.C., Ertl A., Dutrow B., Uher P. and Pezzotta F. (2011) Nomenclature of the tourmaline supergroup minerals. *American Mineralogist*, **96**, 895–913.

Henry D.J., Novák M., Hawthorne F.C., Ertl A., Dutrow B.L., Uher P. and Pezzotta F. (2013) Erratum. *American Mineralogist*, **98**, 524.

Lyckberg P., Chornousenko V. and Wilson W.E. (2009) Famous mineral localities: Volodarsk-Volynski, Zhitomir Oblast, Ukraine. *Mineralogical Record*, **40**, 473–506.

Macey P.H., Ingram B.A., Cronwright M.S., Botha G.A., Roberts M.R., Grantham G.H., de Kock G.S., Maré L.P., Botha P.M.W., Kota M., Opperman R., Haddon I.G., Nolte J.C. and Rower M. (2006) *Map explanation sheets Alto Molócuè (1537), Marrupula (1538), Nampula (1539), Mogincual (1540), Errego (1637), Gilé (1638), and Angoche (1639–40)*. Republic of Mozambique, Ministry of Mineral Resources, National Directorate of Resources, Council for Geoscience, pp. 402.

Mandarino J.A. (1981) The Gladstone-Dale relationship. Part IV: the compatibility concept and its application. *The Canadian Mineralogist*, **19**, 441–450.

Martin R.F. (2024) Cleavelandite: only crystals small and beautiful. *Rocks & Minerals*, **99**, 322–331.

Mattson S.M. and Rossman G.R. (1984) Ferric iron in tourmaline. *Physics and Chemistry of Minerals*, **11**, 225–234.

Mattson S.M. and Rossman G.R. (1987) Fe^{2+}–Fe^{3+} interactions in tourmaline. *Physics and Chemistry of Minerals*, **14**, 163–171.

Pieczka A. and Sęk M. (2017) Bosiite or not bosiite. That is the question. pp. 63–64 in: *Tourmaline 2017 International Symposium, Book of Abstracts*.

Pouchou J.L. and Pichoir F. (1991) Quantitative analysis of homogeneous or stratified microvolumes applying the model "PAP." pp. 31–75 in: *Electron Probe Quantitation* (K.F.J. Heinrich and D.E. Newbury, editors). Plenum, New York.

Prescher C., McCammon C. and Dubrowinsky L. (2012) *MossA*: a program for analyzing energy-domain Mössbauer spectra from conventional and synchrotron sources. *Journal of Applied Crystallography*, **45**, 329–331.

Sabine T.M., Hunter B.A., Sabine W.R. and Ball C.J. (1998) Analytical expressions for the transmission factor and peak shift in absorbing cylindrical specimens. *Journal of Applied Crystallography*, **31**, 47–51.

Sheldrick G.M. (2015) Crystal structure refinement with SHELXL. *Acta Crystallographica*, **C71**, 3–8.

Smith G. (1978) A reassessment of the role of iron in the 5,000–30,000cm^{-1} region of the electronic absorption spectra of tourmaline. *Physics and Chemistry of Minerals*, **3**, 343–373.

Taran M.N. and Rossman G.R. (2002) High-temperature, high-pressure optical spectroscopic study of ferric-iron-bearing tourmaline. *American Mineralogist*, **87**, 1148–1153.

Taran M.N., Lebedev A.S. and Platonov A.N. (1993) Optical absorption spectroscopy of synthetic tourmalines. *Physics and Chemistry of Minerals*, **20**, 209–220.

van Hinsberg V.J., Schumacher J.C., Kearns S., Mason P.R.D. and Franz G. (2006) Hourglass sector zoning in metamorphic tourmaline and resultant major and trace-element fractionation. *American Mineralogist*, **91**, 717–728.

Warr L.N. (2021) IMA–CNMNC approved mineral symbols. *Mineralogical Magazine*, **85**, 291–320.

Watenphul A., Burgdorf M., Schlüter J., Horn I., Malcherek T. and Mihailova B. (2016) Exploring the potential of Raman spectroscopy for crystallo- chemical analyses of complex hydrous silicates: II. Tourmalines. *American Mineralogist*, **101**, 970–985.

Wright S.E., Foley J.A. and Hughes J.M. (2000) Optimization of site occupancies in minerals using quadratic programming. *American Mineralogist*, **85**, 524–531.

Young R.A. (1993) Introduction to the Rietveld method. pp. 1–38 in: *The Rietveld method* (Young R.A., editor). Oxford University Press, UK.